Hydrogen-Assisted Fracture of Stainless Steel

Samantha K. Lawrence, Dorian K. Balch, Grace Yee, Brian P. Somerday
Sandia National Laboratories
Livermore, CA 94551

Abstract

Symmetric four-point bending (S4PB) and anti-symmetric four-point bending (AS4PB) were applied to assess the effect of hydrogen on crack initiation and propagation in a stable, nitrogen-strengthened austenitic stainless steel (21Cr-6Ni-9Mn). Specimens of a high strength aluminum alloy (AA2219-T851), which has also been identified as hydrogen-compatible, were used for test method development prior to completing the stainless steel test matrix. Single edge notched bend (SEN(B)) specimens were extracted from forged 21Cr-6Ni-9Mn bar and AA2219 plate. The 21Cr-6Ni-9Mn specimens were then hydrogen charged with ~200 wt. ppm hydrogen; AA2219 specimens were not charged. Aluminum specimens were tested in S4PB to induced mode I (pure bending), and AS4PB to attain varying levels of mode I/II mixity and mode II (pure shear), where the ratio of mode I to mode II varies with the position of the crack plane relative to the load line. After test method troubleshooting and validation, hydrogen-charged stainless steel specimens were then subjected to mode I and two ratios of mixed mode I/II. Mode II loading was not achieved due to high load limitations. Analyses of fracture profiles for both materials reveal a marked effect of loading mode mixity on initial crack propagation orientation, however a specific contribution of hydrogen was not readily identifiable. Fracture initiation toughness in the presence of hydrogen, J_{IH}, was calculated following the J-integral approach; the mode I J_{IH} calculated for stainless steel samples fractured in S4PB were consistent with published values determined from compact tension specimens. The peak loads required to initiate fracture during AS4PB far exceeded those required during S4PB. This is attributed to the increasing shear force applied to the specimens as the degree of mode mixity increases. Ultimately, understanding the fracture response of hydrogen-exposed stainless steels subjected to mixed mode I/II loading is critical for designing hydrogen containment vessels or gas transfer systems (GTS).

Introduction

The aging-related degradation of stainless steels in hydrogen environments is a well-known problem having a negative impact on the long-term performance of containment materials in hydrogen storage applications. This has direct implications for the safety and reliability of hydrogen isotope containment reservoirs in gas transfer systems (GTS). It is also generally accepted that flaws in containment materials are subjected to mixed loading modes (i.e. multi-axial stress fields), therefore safe design of structural components containing defects or flaws that are inclined relative to the applied stress directions requires an understanding of mixed-mode loading effects on crack initiation and propagation. Mixed mode I/II loading has been identified as particularly important for pressure vessels in hydrogen service. While standard procedures exist for determining mode I (bending) fracture toughness of ductile metals,

this is not the case for mode II (shear) or mixed mode I/II fracture toughness. Several researchers have undertaken studies of fracture behavior under mixed mode I and II loading [1], [2]; few of these studies have focused on elastic-plastic fracture of ductile materials [3], [4] and none have investigated the effect of mixed mode I/II loading on fracture behavior of hydrogen-exposed structural alloys. Some investigations comparing mode I and mode II fracture toughness indicate that the mode II fracture toughness is higher than mode I when material and orientation are held constant [1]. Since pressure vessel design codes are based on mode I fracture toughness, it is important to determine whether this method is truly conservative for hydrogen-containing structures known to contain flaws that are subjected to multi-axial loading.

Approach

The initial approach called for experiments to be performed solely using forged 21Cr-6Ni-9Mn stainless steel (21-6-9), matching the material investigated in a previous fracture mechanics study [5]. The 21-6-9 composition was (in wt. %) 21.0 Cr, 6.7 Ni, 8.9 Mn, 0.23 N, 0.03 C, 0.35 Si, 0.02 P, 0.00004 S, bal Fe. A 64-mm diameter bar of 21-6-9 was longitudinally upset forged to a diameter of 78 mm at a forging temperature of 1200 K. Forging produced a yield strength of approximately 650 MPa and no ferrite was detected in the forging. Additional details on tensile properties of the forging are provided in Ref. [6].

Single edge bend (SEN(B)) specimens for fracture mechanics testing were extracted from the 21-6-9 forging following the ASTM Standard E1820. Samples had a width of 18 mm, gross thickness of 6 mm, and an overall length of 96 mm. Notches were machined into the specimens such that cracks propagated parallel to the circumferential (C) direction (termed L-C orientation). Some of the specimens were also side grooved along the same plane as the notch; specimen thickness in this plane was reduced by approximately 20%. Single edge bend specimens were pre-cracked in fatigue using a MTS 810 servo-hydraulic load frame to produce an initial crack length-to-width ratio of 0.5 or 0.55 for the 21-6-9 and AA2219 specimens, respectively. The maximum stress intensity factor at the end of the pre-cracking procedure was approximately 29 MPa $m^{1/2}$ for the side-grooved specimens and 31 MPa $m^{1/2}$ for the non-side grooved specimens.

Stainless steel specimens were then thermally hydrogen-charged. Samples were loaded in to an A286 stainless steel pressure vessel placed inside a furnace, which was then heated to 573 K and filled with 138 MPa hydrogen gas (99.9999% pure). The charging cycle lasted 24 days and resulted in a uniform distribution of hydrogen across the specimen thickness. This standard procedure typically results in a bulk hydrogen content of ~230 wt. ppm [5]–[7].

Symmetric four-point bending (S4PB) was used to induce pure mode I (bending), while anti-symmetric four-point bending (AS4PB) was employed to apply mixed-mode I/II (bending and shear) loading, and pure mode II (shear) loading. Following the convention enumerated by Maccagno and Knott [8], mixed loading modes were obtained by varying the crack position with respect to the load line (the distance S_0 in Fig. 1) corresponding to the desired ratio of the shearing force, Q, to the bending moment, M. S_0 is

determined by the specimen width, W, the equivalent crack angle, $ß_{eq}$, and the calibration functions for four point bending, Y_I and Y_{II}, respectively:

$$S_0 = W tan ß_{eq} (Y_{II}/Y_I) \quad (1)$$

where tan $ß_{eq}$ is equal to the ratio of the stress intensity factors K_I/K_{II}. Additional details concerning the development of this convention are found in Ref. [8]. Monotonic fracture tests using a displacement rate of 0.25 mm/min were carried out at room temperature with a 90 kN (20,000 lb-f) load cell. Specimens were loaded at $ß_{eq}$ angles of 90° (mode I), 60°, 30°, and 0° (mode II). Decreasing $ß_{eq}$ corresponds to increasing ratios of mode II:I. In all cases, displacement was measured with a displacement gauge and tests were halted after a 20% load drop (corresponding 20% potential increase). Simultaneously, crack length was monitored using the direct current potential drop(DCPD) method described in ASTM Standard E1737.

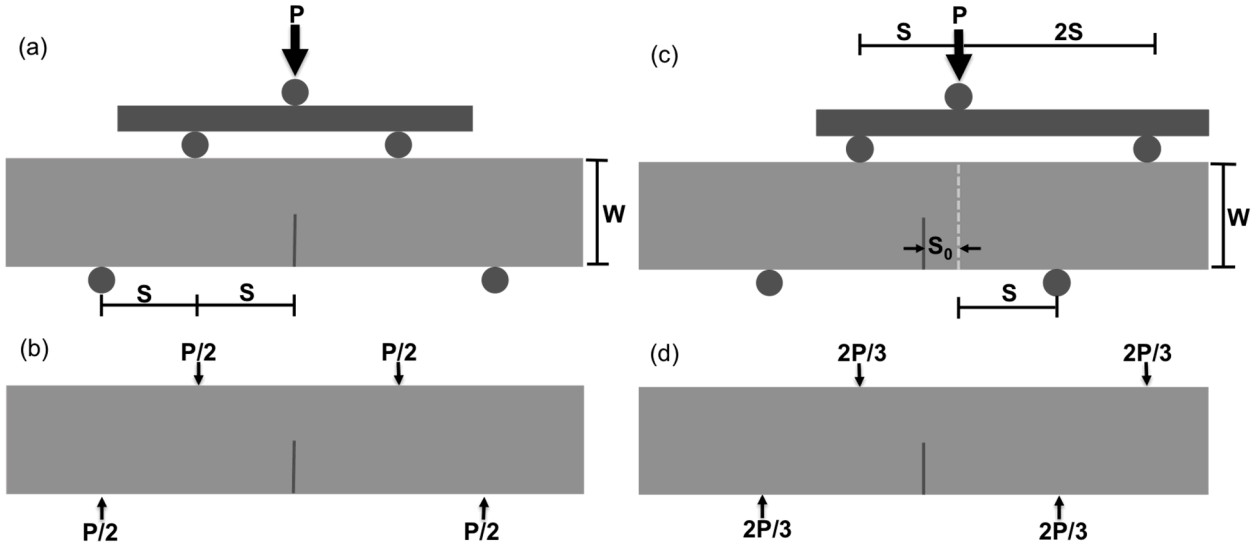

Figure 1: Schematic showing specimen alignment and applied loads for S4PB (a) and (b), and for AS4PB (c) and (d).

A number of problems were encountered during preliminary AS4PB tests, thus an alternate, lower strength material was identified to use for troubleshooting and test method development. A high strength aluminum alloy AA2219 was chosen both for its mechanical properties and because it is a GTS-relevant alloy. A plate (305 mm x 305 mm x 76 mm) of AA2219 in the T851 temper condition was procured from Kaiser Aluminum Fabrication Products. The alloy composition was (in wt. %) 6.5 Cu, 0.008 Mg, 0.29 Mn, 0.05 Zn, 0.03 Ti, 0.07 V, 0.12 Zr, 0.04 Si, 0.1 Fe, bal. Al. and had a reported yield strength of 347.5 MPa, ultimate tensile strength of 455.0 MPa, and elongation of 7.68%. Samples with dimensions identical to the 21-6-9 specimens were extracted from the AA2219 plate such that cracks propagated parallel to the transverse (T) direction (termed L-T orientation). Aluminum specimens were not side grooved, were pre-cracked in fatigue, and were not hydrogen charged.

After successful mode I, mixed mode I/II, and mode II testing using the aluminum specimens, the 21-6-9 test matrix was reinitiated. Two mixed-mode conditions were tested successfully, but pure mode II

loading was not achieved due to load limitations of the servo-hydraulic load frame as well as the bend test fixtures.

Results and Impacts

Mechanical Response to Applied Loads

Load-displacement curves for AA2219 loaded in mode I, mixed mode I/II (60˚ and 30˚), and mode II configurations are presented in Fig. 2. Each specimen exhibited an initial linear elastic response followed by deviation from linear behavior, indicative of significant plasticity. The loads required to propagate a crack increase as the ratio of mode II:I increases; the peak load achieved during 60˚ loading is about 5 times greater than that attained during mode I loading, while the mode II configuration results in a seven-fold increase over the mode I peak load. The changing contributions of shear force versus bending moment are also manifest in the variation of crack opening displacement, δ_I, and sliding displacement, δ_{II}, at the notch root and bottom face. These displacements are given in Table 1 for each loading configuration and were measured directly from photographs like those shown in Fig. 5a-d. Only opening displacement is detected for mode I. Conversely, when samples are subjected to mixed mode I/II loads, both opening and sliding displacements are observed. Under pure mode II loading, shear forces dominate the deformation and, as such, sliding displacements predominate. In general, δ_{II} increases and δ_I decreases as the amount of imposed mode II increases.

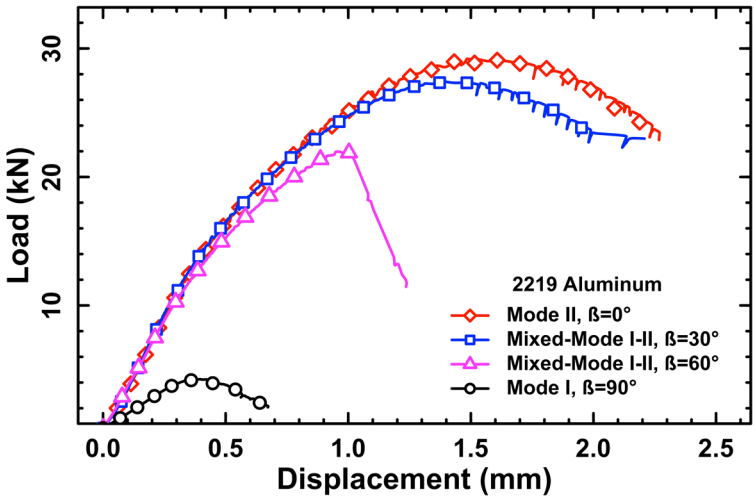

Figure 2: Load-displacement curves for AA2219. The equivalent crack angle, $ß_{eq}$, for each sample is indicated.

Load-displacement curves for 21-6-9 loaded in mode I and mixed mode I/II (60˚ and 30˚) configurations are presented in Fig. 3. Mode II loading was not successful for this material due to load limitations. However, several informative trends are observed. As with the AA2219, significant plasticity occurs after linear elastic loading and the loads required to propagate a crack under mixed-mode conditions are considerably higher than those attained under pure mode I loading; the peak loads achieved during

mixed mode loading are approximately 5 times higher than those induced by mode I. Note that mode I tests were conducted with both side-grooved and non-side grooved specimens to assess the impact of constraint on crack propagation. The peak load achieved for the side-grooved specimen was ~10.5 kN, while the peak load for the non-side grooved specimen was slightly lower, ~8.5 kN. Inspection of the fracture surfaces revealed that side grooving encouraged a more planar crack front and mitigated dimpling on the front and back faces (Fig. 4).

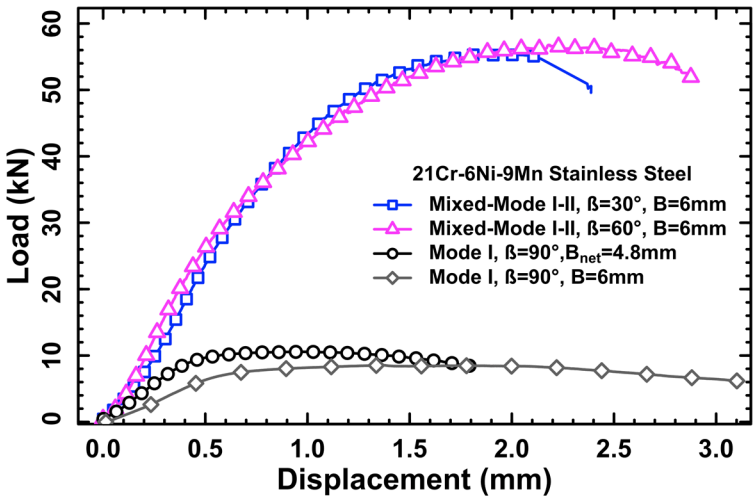

Figure 3: Load-displacement curves for 21Cr-6-Ni-9Mn. The equivalent crack angle, ß$_{eq}$, as well as the net thickness, B, for each sample is indicated.

Crack displacements are also measured as a function of mode mixity. Opening displacement decreases while sliding displacement increases for mixed mode loading, relative to pure mode I (see Table 1). The amount of deformation observed at the crack tip during mixed mode loading is substantial, as shown in Fig. 5e-g by the large vertical displacements of the fiducial scribe lines ahead of the crack tip. While these distortions appear significant, the strain field around the crack tip has not been directly assessed.

Table 1: Crack opening, ∂$_I$, and sliding, ∂$_{II}$, displacements as a function of equivalent crack angle, $ß_{eq}$, for AA2219 and 21-6-9.

		AA2219-T851			21Cr-6Ni-9Mn		
Location	$ß_{eq}$	∂_I	∂_{II}	θ_i	∂_I	∂_{II}	θ_i
Notch Root	0	not measureable		0˚	not tested		
	30	0.135	0.058	30˚	0.051	0.113	9º
	60	0.288	0.841	35˚	0.414	0.856	14º
	90	0.281	N/A	45˚	1.067	N/A	0˚ or 45˚[#]
Bottom Face	0	0.037	0.068		Not tested		
	30	0.174	0.166		0.082	0.141	
	60	0.833	0.826		1.151	0.960	
	90	0.830	N/A		2.365*	N/A	

[#]Note that the constraint imposed by side grooves forced θ_i to be 0º, the non-side grooved specimen resulted in θ_i a of 45º
*Note that ***∂*** was measured using the side grooved 90º 21-6-9 specimen with B_{net} = 4.8mm

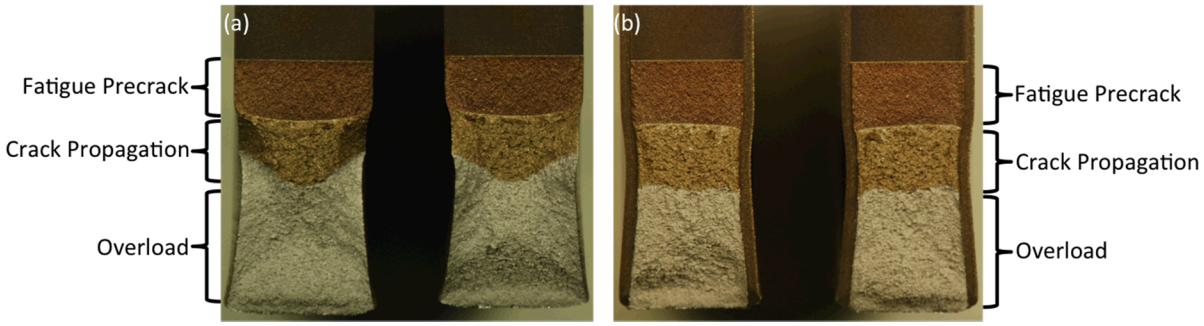

Figure 4: Photographs of 21-6-9 fracture surfaces without side-grooves (a) and with side-grooves (b).

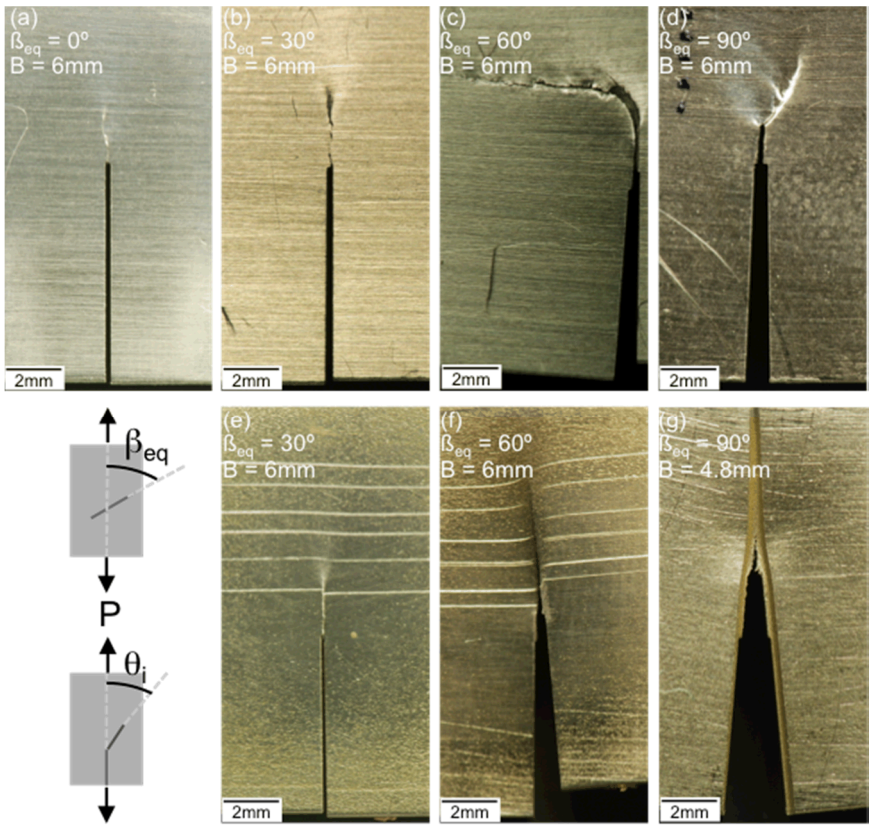

Figure 5: Photographs of fracture profiles for (a-d) AA2219 and (e-g) 21-6-9. The relationship between the applied load, P, and the equivalent crack angle, $ß_{eq}$, and the fracture angle, θ_i, are shown in the bottom left.

Fracture Profiles

Fracture profiles (Fig. 5) were also examined for both aluminum and stainless steel and the angle of the initial portion of the propagating crack was measured with respect to the machined notch. Fracture angles, θ_i, are plotted as a function of equivalent crack angle, $ß_{eq}$, in Fig. 6. For the purposes of this analysis, the starter notch is identified as 0˚. AA2219 specimens loaded to $ß_{eq}$ = 90˚, 60˚, and 30˚ exhibit crack propagation inclined at angles 45˚, 30˚, and 15˚ with respect to the plane of the starter notch,

while specimens loaded in pure mode II evidence cracks propagating parallel to the plane of the notch. That is, fracture angle, θ_i, decreases with increasing mode II, as shown in Table 1.

Fracture angles for the 21-6-9 specimens loaded in mode I and mixed mode I/II are listed in Table 1. As with the aluminum, fracture angle decreases with increasing mode II. Notably, though it is difficult to discern in Fig. 5, a component of mode III (tearing) was applied to the samples loaded at 30˚ and 60˚ near the conclusion of the test.

To determine whether fracture angles correspond with the maximum stress direction, boundaries on maximum shear stress determined using a formalism introduced by Shih[9] are also plotted on Fig. 6 (shaded area). This formalism can be applied even though considerable plasticity occurs in the vicinity of the crack tip and is determined by plotting the normalized shear stress component, $\widetilde{\sigma_{r\theta}}$, against the polar coordinate, θ, in a range of mode I to mode II. Shih develops plots for three Hutchinson strain hardening exponents, *n*. Tensile data for 21-6-9 most closely resembles curves for n=13, hence this value is used to determine the upper and lower bounds of the grey shaded area in Fig. 6 representing the region where the normalized shear stress is a maximum and dominates crackextension. The θ_i values for β_{eq} = 0˚, 30˚, and 60˚ lie comfortably within the maximum shear stress bounds, suggesting that the fracture angles produced by mixed mode loading correspond with a direction of maximum shear stress. Conversely, the 90˚ (mode I) fracture angle lies well outside the bounds, confirming that fracture in this configuration is driven by tensile stresses, rather than shear stresses. The 45˚ fracture profile corresponds with shear lip formation. It is important to note that shear lip formation at the occluded plane is not driven by shear stresses, rather bending moment dominates mode I fracture. While the shear-dominated failures are more striking it is important to remember that a five- to seven-fold increase in applied loads are required to propagate cracks in these configurations. In general, then, designing for bending (tensile)-dominated failure is conservative.

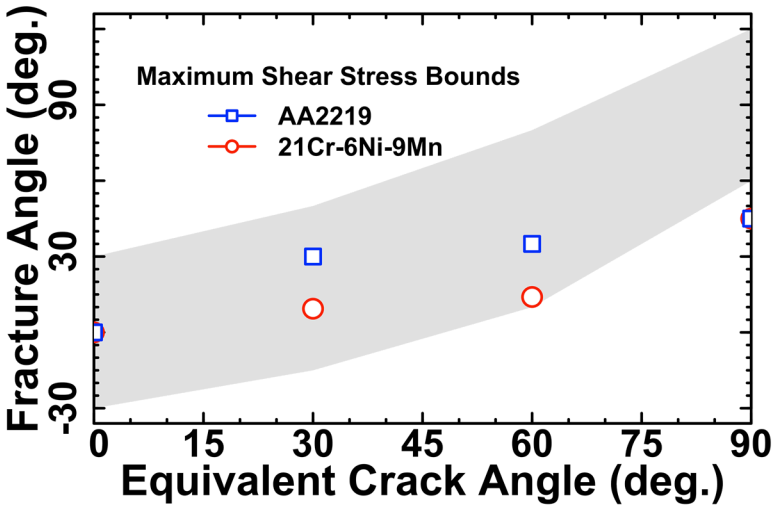

Figure 6: Experimental values of fracture angle compared with the region over which the normalized shear stress is a maximum (shaded grey), based on [2], [9]**.**

J-integral for Mode I Fracture Toughness

Inspection of the images presented in Fig. 5 reveal that considerable plasticityoccurs near the crack tip during mode I and mixed mode loading of 21-6-9 stainless steel, hence a conventional analysis of the linear elastic stress field is not possible. However, a J-integral approach has been successfully applied to determine mode I fracture toughness of hydrogen-charged 21-6-9 using compact tension (CT) specimens [5]. This method can also be applied to calculate mode I fracture toughness of specimens loaded in S4PB following the elastic-plastic methods described in ASTM Standard 1820-09 and using J solutions for the S4PB configuration. The mode I fracture initiation toughness in the presence of hydrogen, J_{IH}, is determined by plotting J vs crack extension, Δa (Fig. 7); the intersection of this curve with a 0.2mm crack blunting line is J_{IH}. This value varies between 295 kJ/m^2 and 310 kJ/m^2 for specimens without and with side grooves, respectively. These values are consistent with the fracture toughness value of 243 kJ/m^2 calculated by Nibur et al. [5] for this alloy. Note that in the current study samples machined both with and side grooves satisfied the thickness criterion for plane strain, however, samples without side grooves developed shear lips during crack propagation. The J-integral for samples loaded in mode II and mixed mode I/II has not yet been determined as finite element modeling is required to calculate the geometry-dependent stress intensity factors and calibration functions, as has been described by other researchers [10]. However, it is important to recognize that the calculated J_{IH} for hydrogen-charged 21-6-9 is still remarkably high. For comparison, the threshold stress intensity factor, K_{JH}, for hydrogen-charged A286 stainless steel, an alloy that performs reliably in high-pressure hydrogen gas, is ~90 MPa m$^{1/2}$ [11], while the for K_{JH} of 21-6-9 estimated from J in this study exceeds 200 MPa m$^{1/2}$.

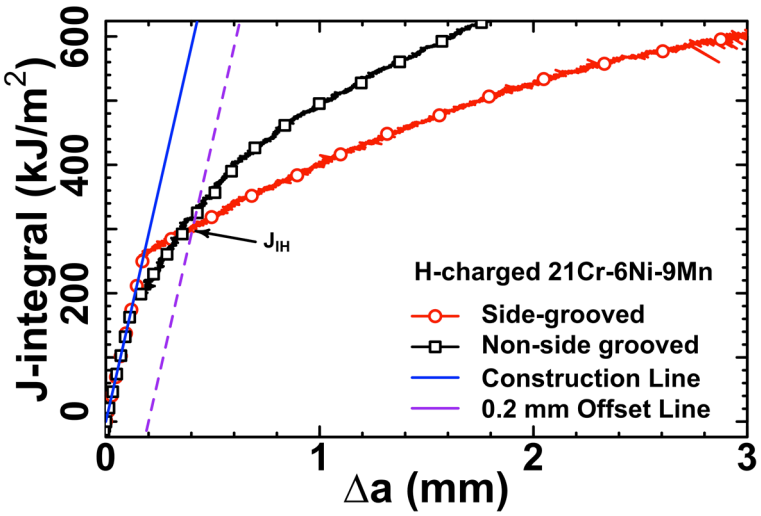

Figure 7: *J-integral* vs crack extension, Δa, curves for hydrogen-charged 21-6-9 with and without side-grooves.

Challenges Encountered during Test Method Application

A number of challenges were encountered during the development and application of AS4PB that contribute to error in the measured data. Chief among thesechallenges were fixture alignment and specimen alignment. Any movement of the crosshead or actuator produced subtle changes in the

alignment of the top and bottom fixtures with respect to each other, which had a dramatic effect on the "alignment" of the applied load. Slight fixture misalignments led to asymmetric pinching of the specimen, resulting in, at best, a sample that "leaned" forward or backward slightly at high loads and experienced some component of mode III loading, and at worst, a sample that pinched so severely as to be ejected from the load train. Coupled with vertical fixture alignment, lateral roller alignment also impacted the success of a particular test. Because the fixtures used in the current investigation were a "continuous" rather than "discrete" set-up, to borrow terminology used by Laukkanen [10], rollers were positioned and aligned manually on a millimeter scale. A concerted effort was made to ensure the rollers were positioned relative to the zero-point of the load train, but slight misalignment due to the manual procedure was likely. Additionally, the applied forces during mixed mode loading are substantially higher than mode I because shear forces induced by the mixed-mode configuration create a two-dimensional displacement field. High applied forces can deform not only the specimen, but also the rollers and roller supports. Friction between the specimen and the rollers also contribute measurement error. In order to circumvent these kinds of alignment issues, discrete test setups should be used when possible; a more rigid load train, such as that described by Tohgo et al. [4] would also likely mitigate asymmetric sample pinching.

Specimen misalignment, with respect to the fixtures, can be laborious, but is fundamentally important to data quality. While variation in the distance of the pre-crack from the load line will produce commensurate variation in the ratio of mode I/II loading applied, any specimen rotation laterally about the load line exacerbates misalignment between the top and bottom fixtures and can induce additional or premature asymmetric pinching. Manual specimen alignment with the millimeter scale on the fixtures was found to be insufficient for repeatable loading tests, thus alignment jigs were designed to aid in proper specimen positioning. Again, a discrete setup would mitigate this issue by incorporating a built-in alignment jig, ensuring accurate and repeatable specimen positioning.

One additional source of ambiguity in measurement lies in the application of DCPD to analyze crack extension. DCPD data were collected, but no readily identifiable trends relating crack extension to loading were observed. For example, as shown in Fig. 8 mixed mode I/II loading produced multiple "knees" or increases in the potential drop curves. During mode I loading, only a single increasing deviation occurs, which corresponds with initial crack extension. The multiple deviations observed in the mixed mode curves do not seem to directly correspond with crack initiation or propagation; crack closure or crack face shearing induced by high shear stresses obfuscate the interpretation of the potential drop data. The reader is referred to Laukkanen's manuscript [10] for review of the difficulties associated with interpreting potential drop data in mixed mode testing.

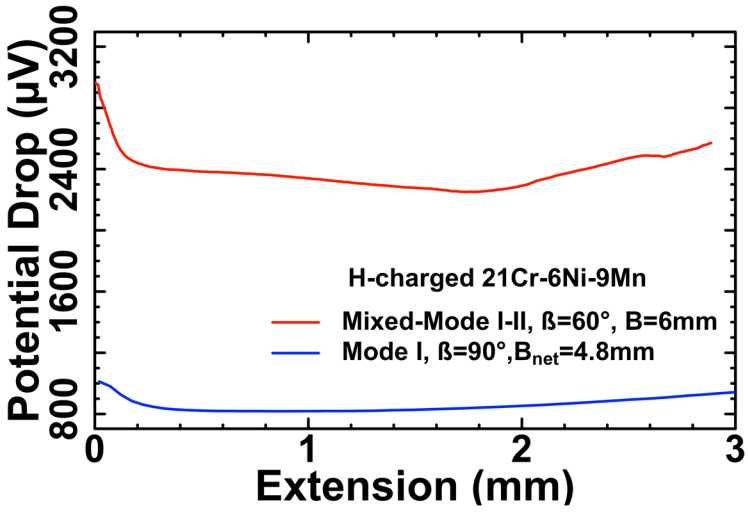

Figure 8: Potential drop curves obtained with DCPD method for hydrogen-charged 21-6-9 under pure mode I loading and 60˚ mixed mode I/II loading.

Conclusions and Future Work

This year, the applicability of symmetric four-point bending, to induce mode I loading, and anti-symmetric four-point bending, to induce mixed mode I/II and mode II loading, of hydrogen charged 21Cr-6Ni-9Mn stainless steel were assessed. As part of this assessment, test method development was conducted using AA2219-T851 aluminum, because it has lower fracture toughness than austenitic stainless steels, but is still relevant for hydrogen storage and distribution systems. A number of difficulties were encountered in testing 21-6-9 (especially) in AS4PB. These challenges stem from the two-dimensionality of the displacement field imposed by mixed mode loading. Load frame compliance and continuous fixture set-ups exacerbate the two-dimensionality problem. Despite these challenges, valuable data were collected for both alloys. Notably, the mode I fracture toughness of hydrogen charged 21-6-9 exceeded 200 kJ/m^2, a remarkably high value compared with other stainless steels used in hydrogen service. Additionally, for both AA2219 and hydrogen-charged 21-6-9, the addition of shear forces (mode II) to the loading mode substantially increased the applied forces required to extend a crack. Though J-integrals were not computed for the mixed mode configurations, it appears that mode I fracture toughness is a conservative design metric when defects are inclined relative to the applied load. Future work will include comprehensive fractography of 21Cr-6Ni-9Mn specimens fractured under mixed-mode I/II conditions as well as additional microscopy of local deformation ahead of the crack tip in an effort to link hydrogen-deformation interactions with fracture mode under various mixed-mode loading conditions. Finite element modeling to determine the appropriate J-integrals for mixed-mode and pure mode II conditions are desired.

Summary of Findings and Capabilities Related to Aging

- Applied forces required to propagate a crack under any component of shear loading are considerably higher than those required to propagate a crack under bending-dominated loading.

Based on this finding it appears that designing pressure vessels based on mode I fracture toughness values (as is the case in the GTS design guide) is, in fact, conservative.

Acknowledgement

Sandia National Laboratories is a multi-mission laboratory managed and operated by Sandia Corporation, a wholly owned subsidiary of Lockheed Martin Corporation, for the U.S. Department of Energy's National Nuclear Security Administration under contract DE-AC04-94AL85000.

References

[1] Y. W. Shi, N. N. Zhou, and J. X. Zhang, "Comparison of mode I and mode II elastic-plastic fracture toughness for two low alloyed high strength steels," *Int. J. Fract.*, vol. 68, no. 1, pp. 89–97, 1994.

[2] T. M. Maccagno and J. F. Knott, "The Mixed Mode I / II Fracture Behaviour of Lightly Tempered HY 130 Steel At Room Temperature," *Eng. Fract. Mech.*, vol. 41, no. 6, pp. 805–820, 1992.

[3] S. Aoki, K. Kishimoto, T. Yoshida, M. Sakata, and H. A. Richard, "Elastic-plastic fracture behavior of an aluminum alloy under mixed mode loading," *J. Mech. Phys. Solids*, vol. 38, no. 2, pp. 195–213, 1990.

[4] K. Tohgo and H. Ishii, "Elastic-plastic fracture toughness test under mixed mode I-II loading," *Eng. Fract. Mech.*, vol. 41, no. 4, pp. 529–540, 1992.

[5] K. A. Nibur, B. P. Somerday, D. K. Balch, and C. S. Marchi, "The role of localized deformation in hydrogen-assisted crack propagation in 21Cr – 6Ni – 9Mn stainless steel," *Acta Mater.*, vol. 57, no. 13, pp. 3795–3809, 2009.

[6] C. San Marchi, D. K. Balch, K. Nibur, and B. P. Somerday, "Effect of High-Pressure Hydrogen gas on Fracture of Austenitic Steels," *J. Press. Vessel Technol.*, vol. 130, no. 4, pp. 41401–1--9, 2008.

[7] B. P. Somerday, M. Dadfarnia, D. K. Balch, K. A. Nibur, C. H. Cadden, and P. Sofronis, "Hydrogen-Assisted crack propagation in austenitic stainless steel fusion welds," *Metall. Mater. Trans. A Phys. Metall. Mater. Sci.*, vol. 40, no. 10, pp. 2350–2362, 2009.

[8] T. M. Maccagno and J. F. Knott, "The fracture behavior of PMMA in mixed modes I and II," *Eng. Fract. Mech.*, vol. 34, no. 1, pp. 65–86, 1989.

[9] C. F. Shih, "Small-Scale Yielding Analysis of Mixed Mode Plane-Strain Crack Problems," in *Fracture Analysis*, 1974, vol. STP 560, pp. 187–210.

[10] A. Laukkanen, "Analysis of experimental factors in elastic-plastic small specimen mixed-mode I-II fracture mechanical testing," *Fatigue Fract. Eng. Mater. Struct.*, vol. 24, no. 3, pp. 193–206, 2001.

[11] M. W. Perra, "Sustained-load Cracking of austenitic Steels in Gaseous Hydrogen," in *Environmental Degradation of Engineering Materials in Hydrogen*, 1981, pp. 321–333.

Administrative Addendum

Related Publications and Presentations:

S.K. Lawrence, B.P. Somerday, G. Yee, D.K. Balch: Mixed Mode Fracture Toughness Testing of Hydrogen-charged 21Cr-6Ni-9Mn Stainless Steel and AA2219 Aluminum. *Proceedings of the 2016 International Hydrogen Conference* (submitted)

Contributed Poster: S.K. Lawrence, B.P. Somerday, G. Yee, D.K. Balch "Mixed Mode Fracture Toughness Testing of Hydrogen-Charged 21Cr-6Ni-9Mn Stainless Steel", 2016 International Hydrogen Conference, Jackson WY, Sept. 11-14, 2016.

Milestone Status:

1. Complete measurements of hydrogen-assisted cracking susceptibility of 21Cr-6Ni-9Mn stainless steel forging under range of mode I-mode II loading combinations (06/30/2016)

   This task has been completed; the results have been compiled into a manuscript for the proceedings of the 2016 International Hydrogen Conference and were presented at that conference.

2. Complete characterization of deformation microstructures in 21-6-9 stainless steel forging as function of temperature and hydrogen concentration (09/30/2016)

   This task was not extended beyond the results reported previously due to extensive complications and delays associated with machining and testing the 21-6-9 specimens under mode I and mode II loading. Samples are now available both fractography and high-resolution microscopy, similar to that described in the FY15 ESAR.

Acronym/Abbreviation List

AA2219	Aluminum alloy 2219
AS4PB	Anti-symmetric four-point bending
S4PB	Symmetric four-point bending
SEN (B)	Single edge notched bending specimen
21-6-9	21Cr-6Ni-9Mn stainless steel
$ß_{eq}$	Equivalent crack angle
θ_I	Initial crack propagation angle

∂_I	Crack opening displacement
∂_{II}	Crack sliding displacement
J_{IH}	Mode I fracture initiation toughness in the presence of hydrogen